POLITECNICO DI TORINO
Repository ISTITUZIONALE

Monitoring the injection of microscale zerovalent iron particles for groundwater remediation by means of complex electrical conductivity imaging

(Article begins on next page)

10 April 2024

Monitoring the injection of microscale zero-valent iron particles for groundwater remediation by means of complex electrical conductivity imaging

Adrián Flores Orozco [1)], Milica Velimirovic [2),+], Tiziana Tosco [3)], Andreas Kemna [4)], Hans Sapion [5)], Norbert Klaas [6)], Rajandrea Sethi [3)], and Bastiaens Leen [2)]*

1) Geophysics Research Group, Vienna University of Technology, Gusshausstraße 27-29, E120-3, 1040 Vienna, Austria

2) Flemish Institute for Technological Research (VITO), Boeretang 200, 2400, Mol, Belgium;
+ Department of Environmental Geosciences, University of Vienna, Althanstrasse 14, 1090, Vienna, Austria.

3) DIATI - Dipartimento di Ingegneria del Territorio, dell'Ambiente e delle Infrastrutture, Politecnico di Torino, Corso Duca degli Abruzzi 24, 10129 Torino – Italy

4) Department of Geophysics, Steinmann Institute, University of Bonn, Meckenheimer Allee 176, 53115 Bonn, Germany

5) SAPION, Oude Bevelsesteenweg 51, 2560 Nijlen, Belgium

6) VEGAS, University of Stuttgart, Pfaffenwaldring 61, 70569 Stuttgart, Germany

*Corresponding author e-mail address: adrian.flores-orozco@geo.tuwien.ac.at

Abstract

The injection of microscale zero-valent iron particles (mZVI) for groundwater remediation has received much interest in recent years. However, to date, monitoring of mZVI particle injection is based on chemical analysis of groundwater and soil samples and, thus, might be limited in its spatio-temporal resolution. To overcome this deficiency, in this study we investigate the application of complex electrical conductivity imaging, a geophysical method, to monitor the high-pressure injection of mZVI in a field-scale application. The resulting electrical images revealed an increase in the induced electrical polarization (~20%), upon delivery of ZVI into the targeted area, due to the accumulation of metallic surfaces at which the polarization takes place. Furthermore, larger changes (>50%) occurred in shallow sediments, a few meters away from the injection, suggesting the migration of particles through preferential flowpaths. Correlation of the electrical response and geochemical data, in particular the analysis of recovered cores from drilling after the injection, confirmed the migration of particles (and stabilizing solution) to shallow areas through fractures formed during the injection. Hence, our results demonstrate the suitability of the complex conductivity imaging method to monitor the transport of mZVI during subsurface amendment in quasi real-time.

Keywords

1. Introduction

Recent research addresses the injection of reactive nano- and micro-scale particles into the subsurface for the stimulated in-situ degradation of pollutants present in aquifers[1]. Particles may be injected directly into the targeted contaminated zone, or close to the source of contamination for deep plumes, decreasing the remediation time, but also permitting the remediation of areas not accessible with other techniques, such as underneath buildings, deep contaminant plumes, or areas characterized by low hydraulic conductivity[2, 3, 4]. Furthermore, in-situ site remediation is significantly faster compared to other conventional approaches[5]. In particular, microscale zero-valent iron (mZVI) particles have received much attention for field applications due to their lower costs and extended longevity in comparison with nano-sized ZVI (nZVI) particles[6, 7]. Although promising, the main difficulty of this remediation technique is related to the successful delivery of the ZVI into the subsurface. Injected ZVI particles are prone to rapid aggregation due to strong non-DLVO magnetic attraction forces (particularly nZVI)[8, 9], sedimentation (particularly for mZVI)[10, 11], and oxidation[12]; and causing a loss in reactivity and decreased mobility, thus limiting the efficacy of the remediation[4, 5]. To overcome this deficiency, different studies have explored the coating of ZVI particles with different surface modifiers[1, 13]. An alternative approach consists in the dispersion of mZVI particles in viscous non-Newtonian fluids[11, 14] to increase stability. Laboratory studies have demonstrated that solutions of biopolymers (e.g., guar gum) are effective in this sense, reducing sedimentation and aggregation[3, 11, 14]. Recent experiments at the field scale have demonstrated the enhanced stability of guar gum (GG) coated mZVI particles (hereafter GG-mZVI), with particles migrating over several meters from the injection point[3].

To date, the monitoring of ZVI particle injection is performed through geochemical analysis of soil and water samples[3, 5]. Although geochemical analyses provide direct and precise measurements of the properties of interest, they are strongly limited by the characteristics of the samples (e.g., location of the boreholes, sampling volumes and rates) and, thus, the spatial resolution of the monitoring results. Moreover, sample collection and chemical analyses are time-consuming, and not suitable for real-time monitoring of field activities, like reagent delivery. Furthermore, one of the main advantages of the remediation through ZVI amendment is its applicability in aquifers characterized by low hydraulic conductivity. Here, the injection is performed at high pressure, in order to create preferential flow paths (fractures)[3, 15]. Particle injection via fracturing is also required in aquifers characterized by sediments with pore size comparable to particle size[16]. In this case, the geochemical monitoring may be limited by the distribution of sampling wells, as well as by the geometry and location of the fractures controlling the flow, relevant to water sampling. Therefore,

the application of mZVI for subsurface remediation urges the development of a monitoring technique, able to track the migration path of the particles, to delineate the extension and distribution of the iron slurry, as well as to characterize processes accompanying particle injection, such as aggregation, oxidation and clogging[5]. Geophysical methods seem to be a suitable alternative to conventional approaches, as they permit to obtain continuous information on the subsurface electrical properties based on non-invasive measurements performed on the surface or in existing boreholes[17]. Although geophysical methods may provide information with enhanced spatio-temporal resolution, geochemical data (from water and soil analyses) are still required to calibrate models linking the geophysical properties with parameters of interest (e.g., ZVI volumetric-content, contaminant concentrations).

Given the strong induced electrical polarization response observed in presence of electronic conductors (e.g., metallic minerals), the complex electrical conductivity method, or simply complex conductivity (CC), has been stablished as a standard tool for the exploration of metallic ores[18]. Taking this into account, CC images resulting from tomographic surveys have been utilized to evaluate changes in the reactivity of ZVI permeable reactive barriers[19] (PRB), and to assess changes in pore-space geometry due to the accumulation of metallic minerals following biostimulation[20, 21]. Furthermore, due to the sensitivity of the CC to geochemical processes taking place at the mineral grain-water interface, CC imaging has been successfully applied at the field scale to delineate changes in the dominating redox-status of sediments in the course of bioremediation[21, 22] and to discriminate between the source zone and the plume for hydrocarbon contaminants[23].

A recent study by Joyce et al. (2012)[24] investigated the CC response in laboratory experiments due to different metallic nanoparticles in a sand matrix. Their study reported an increase in the polarization effect for silver (Ag) and ZVI particles with increasing particle concentration, whereas a negligible polarization response was observed for metallic oxides. However, their study was performed on bare nano-scale particles, without any coating or solution to increase the stability of the particles To our knowledge, to date there is no study investigating the applicability of the CC imaging method to monitor the injection of stabilized mZVI at the field scale. In particular, experiments at the field scale are required to investigate the signal strength and the electrical response for measurements during the injection of stabilized mZVI.

The present study reports the application of the CC imaging method to characterize the delivery of guar gum stabilized mZVI (GG-mZVI) during a field-scale injection by hydraulic fracturing. Our objective is to evaluate the application of CC monitoring images to delineate the migration pathway of the injected mZVI. Particles injection was conducted in the framework of the EU FP7-

AQUAREHAB project along with geochemical monitoring, which was recently reported in detail[3]. We hypothesize that the comparison of the electrical images obtained at different steps during and after the injection of GG-mZVI provides information on the migration pathway followed by the particles, associated with an increase in the polarization response due to the accumulation of metallic surfaces, e.g., ZVI. Due to the lack of a generally accepted petrophysical model linking geochemical parameters (e.g., contaminant concentration) and the electrical response, this study is not designed to explore the long-term effect in the contaminant plume. Instead, we focus on the imaging results obtained during the delivery of GG-mZVI and 12 hours after the injection was concluded.

2. Material and methods

2.1. Study area

The site is located in an industry area in Belgium, where the production of solvent-based painting and coating led to a severe contamination of the aquifer, mainly by chlorinated aliphatic hydrocarbons (CAHs), in particular trichloroethene (TCE) and 1,1,1-trichloroethane (1,1,1-TCA). Initial hydrogeological characterization of the site revealed three main units: a shallow sandy unit (0 to 4.5 m depth), followed by a clayey-sandy aquitard (4.5 to 8 m depth) and a deeper aquifer consisting of fine sands (8 to 20 m depth). According to an analysis of the aquifer sediments recovered during the installation of monitoring wells, individual grains of glauconite are present in materials below 5 m depth. Groundwater was located at 2.5 m below ground surface (bgs), with a flow direction toward south-southwest, and an estimated flow velocity of ~10 m/year. Pumping and slug tests performed at the site[3] estimated an average hydraulic conductivity of 8.2 x 10^{-5} m/s for the aquifer (depth > 8 m bgs) and 2.4 x 10^{-6} m/s for the clayey-sandy aquitard. Analysis of recovered sediments from the deep aquifer reported a grain size distribution of d_{10} = 52 μm and d_{90} = 374 μm, and an effective porosity of 18%. A complete description of the chemical composition of groundwater is presented in Table 1.

Geochemical analysis of water samples collected previously at the site reported that the 1,1,1-TCA plume reaches a depth of 13.5 m bgs, while the TCE plume reaches 15.5 m bgs. The distribution of the TCE, 1,1,1-TCA and 1,1-dichloroethane (1,1-DCA) plumes for concentrations above 1 mg/L are presented in Figure 1, as obtained from the interpolation of existing data. Further details of the site can be found in a previous study[3].
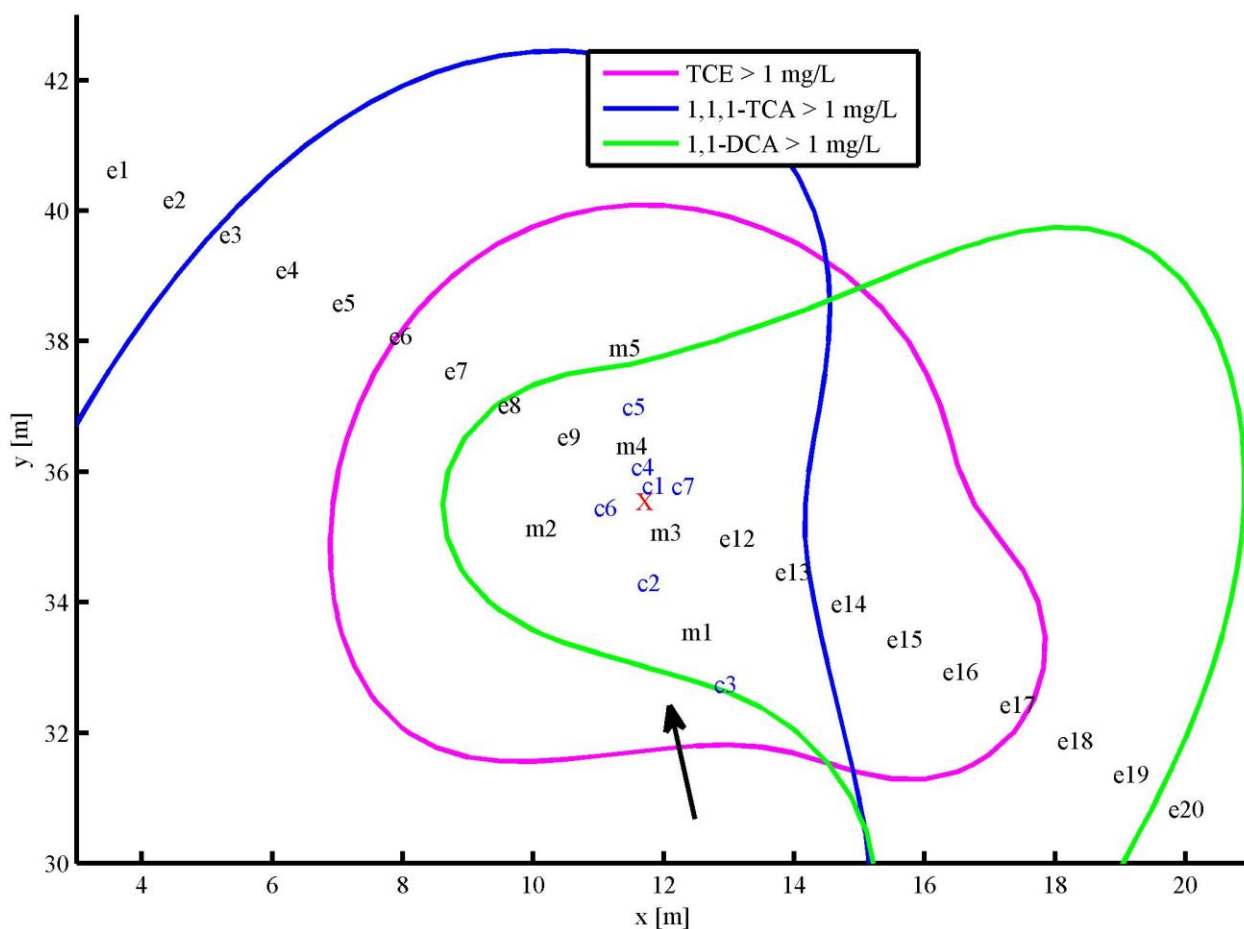
Figure1: Schematic representation of the experimental set-up, with the position of the mZVI-injection point indicated by the red cross. The extension of the contaminant plumes for concentrations above 1 mg/L are indicated by the contour lines. The arrow indicates the groundwater flow direction. The position of the electrodes (e1, e2, etc.), the multilevel samplers (MLS) (m1 – m5) and the core samplers (CS) (c1 – c7) is indicated by the respective initial letters.

Table 1: The chemical composition of groundwater reported at the test site. The field parameters were measured in water samples using a Multimeter Multi 340i WTW Germany with following components: a pH electrode SenTix41 (for pH measurements), a conductivity measuring cell TetraCon 325 (for measurements of the electrical fluid conductivity), an oxygen sensor Cell0x 325, and Liq-Glass ORP electrodes from Hamilton-Nevada (for oxidation-reduction potential).

Field parameters	Unit	
temperature	°C	12.5 ± 0.1
pH		5.75 ± 0.02
ORP	mV	-56 ± 10
Conductivity	mS m^{-1}	85.8 ± 0
Dissolved O$_2$	mg L^{-1}	0.59 ± 0.07
Redox parameters	**Unit**	
CO$_3^{2-}$	mg L^{-1}	n.d.
HCO$_3^-$	mg L^{-1}	82.3
Dissolved Ca	mg L^{-1}	34.2
Dissolved Fe	mg L^{-1}	121
Dissolved Mn	mg L^{-1}	0.62
Cl$^-$	mg L^{-1}	114
SO$_4^{2-}$	mg L^{-1}	201

2.2. GG-mZVI injection

Subsurface amendment in this study targeted the materials underlying the known source zone (Figure 1). A total volume of 1.5 m^3 GG-mZVI was injected into the subsurface, consisting of 70 g/L mZVI, and 7 g/L guar gum (HV7000, Rantec). Injections were performed at high pressure from bottom to top at 10.5, 10.0, 9.5, 9.0 and 8.5 m bgs, with an average of ~21 kg injected mZVI at each depth. Each injection lasted approximately 15 minutes, with 15 minute periods between successive injections to move the pump to the next injection depth. The employed reactive mZVI particles are reported to have a particle size distribution of d_{10} = 24 µm, d_{50} = 56 µm, d_{90} = 69 µm, and specific surface areas according to Burnauer-Emmett-Teller (BET) of 57 m^2/kg. Enzymes (LEB-H, Rantec) were added to the pump tank at the end of each injection period in order to induce fast degradation of the guar gum for the recovery of mZVI reactivity [3, 7, 25].

2.3. Laboratory tests

Relevant properties of the GG-mZVI slurry were measured in the laboratory on slurry similar to that injected in the field, prepared using tap water. Electrical conductivity of GG solution with and without mZVI particles, prior and after enzyme addition, was measured using a multi-parameter probe. Zeta-potential of mZVI particles dispersed in GG prior and after enzyme addition was measured using an acoustic spectrometer (DT. 1200, Dispersion Technology Inc.).

2.4. Geochemical monitoring

Groundwater samples before and after GG-mZVI injection were collected at depths of 4.5, 8.0, 8.5, 9.0, 9.5, 10.0, and 10.5 m bgs by means of multilevel samplers (MLS) located at the positions shown in Figure 1. To better assess the distribution of the injected mZVI, a total of seven core samples (CS) were collected after stopping the mZVI amendment, located at the positions shown in Figure 1. ZVI-concentrations in the recovered core-samples were quantified trough hydrogen measurements after acid digestion of sub-samples[3].

2.5. Complex Conductivity Imaging

The CC method - also known as induced polarization (IP) method - is based on four-electrode impedance measurements, where two electrodes are used to inject electric current and the other two to measure the resulting voltage. In the present study, measurements were collected in the time-domain, where the injected current signal is a square wave with on and off times. Here, CC

measurements are given by the ratio of the recorded voltage to the injected current amplitude (resistance), and the measurement of the voltage decay, once the current is switched off (chargeability). Inversion of tomographic datasets collected with tens of electrodes, provides the distribution of the CC (σ^*) in the subsurface[17]. The resulting images can be expressed in terms of the real (σ') and imaginary (σ'') components of the CC; or, alternatively, by its magnitude ($|\sigma|$) and phase (ϕ). The CC can also be described in terms of its inverse, the complex resistivity, ρ^* ($\rho^*=1/\sigma^*$).

The real component (σ'), or magnitude ($|\sigma|$), of the CC is mainly controlled by the electrical conductivity of the fluid (σ_f), porosity, and the connectivity of the pore space[26], and to a lesser extent to surface conductivity (σ_s) in presence of metallic minerals (i.e., particles). The imaginary component of the CC (σ'') is solely related to surface conductivity (i.e., interface polarization effects), which arise due to electrochemical processes taking place at the interface between mineral grains and pore fluid.

Strong polarization effects are related to the presence of metallic minerals (or particles) in contact with an electrolyte. Here, the application of an external electrical field induces oxidation-reduction reactions at the metal-electrolyte interface, involving charge transfer mechanisms from ionic to electronic: in the forward half reaction, a metal ion in solution accepts an electron from the metal and is reduced to the atomic state, while at another location of the metal, the reverse process takes place[18]. Laboratory measurements[24] have revealed a measurable induced polarization response for ZVI nanoparticles in a sand matrix, with increasing phase values (ϕ) for increasing particle concentrations. However, we note here that in the study of Joyce et al. (2012)[24], the nanoparticles were mixed to the sand during the preparation, i.e., they did neither consider the injection of particles nor the effect of the stabilizing solution.

In the present study, tomographic CC surveys were conducted with a Syscal Pro (Iris Instruments) using 24 stainless steel electrodes at a separation of 1 m along a surface transect (see Figure 1). Data were collected using a dipole-dipole configuration, which combines "skip-3", "skip-4" and "skip-5" measurements with dipole lengths of 4, 5 and 6 m, respectively (i.e., dipole length defined by the number of skipped electrodes along the electrode array). The selection of the measurement configurations plays a key role regarding the resolution and depth of investigation of the imaging results. Usually the aim is to find the best compromise between signal-to-noise ratio (favored by large dipole lengths), image resolution (favored by small dipole lengths) and depth of investigation (favored by larger separation between the current and potential dipoles). Hence, the use of a reduced number of measurements will reduce the time required for data collection, but also the

resolution of the resulting images. Further details on the characteristics of different measurement configurations can be found in other studies[17, 21, 27, 28].

The measurement protocol was carefully designed to minimize electromagnetic coupling, avoid voltage measurements using electrodes previously used for current injection[21], and increase the signal-to-noise ratio for deep measurements. For the particular purpose of this study, it was important to collect an entire data set in less than 15 minutes, which was the time required, after each injection, to relocate the injection pump to the next depth. The intended exploration depth was 11 m, considering the maximal depth of the particle injection of 10.5 m. Initial and final measurements were collected as normal and reciprocal pairs for quantification of the data error, where a reciprocal reading consists in the repetition of the measurements after interchanging current and potential dipoles. Monitoring measurements collected during particle injection were performed only as normal readings, to reduce acquisition time. A square-wave current (50% duty cycle) was injected with a pulse length of 2 s. Integral chargeability measurements were obtained through 20 voltage readings recorded between 240 and 1.840 ms after current shut-off. We note here that it was impossible to increase the length of the profile to avoid the vicinity of walls and other sources of anthropogenic noise. Shorter separation of electrodes would have increased the resolution in shallow areas but undesirably increased the acquisition time. For the purpose of this study, we opted for a single 2D profile, given the significantly increased acquisition time associated with 3D surveys.

The electrical images were computed with CRTomo, a smoothness-constraint inversion algorithm by Kemna (2000)[27]. To enhance the quality of the inverted images, data-error parameters were defined in the inversion as stopping criterion. Data error was quantified based on the analysis of normal-reciprocal discrepancies, as described in a previous study[28]. For the inversion of time-domain measurements, chargeability values were linearly converted to frequency-domain phase values (at the fundamental frequency of 0.125 Hz), which assumes a constant-phase response[27]. This approach has been demonstrated to provide accurate results in previous studies[23]. Although not discussed here, we also tested inversions with other regularization schemes[29]. However, these results revealed no improvement over the images computed with the standard smoothness-constraint regularization and adequate data-error quantification, as presented here.

3. Results and Discussion

3.1. CC imaging for CAH plume characterization: in situ CAHs targeting

Figure 2 shows the CC imaging results and geochemical parameters (i.e., σ_f, TCE and 1,1,1-TCA concentrations) for the data collected one day before the GG-mZVI injection in MLS. The CC is presented in terms of real (σ') and imaginary (σ'') components, as well as phase (ϕ). To guide the interpretation of the electrical images, we marked the interfaces between the lithological units.
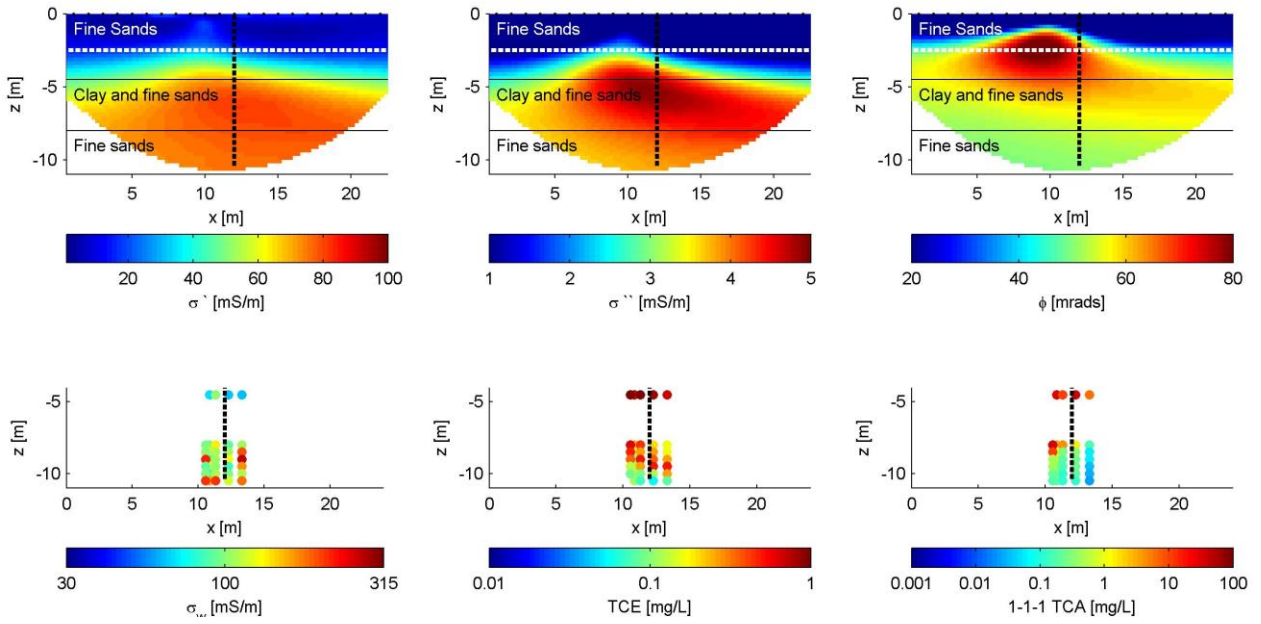

Figure 2: Electrical imaging results for data collected before the injection of GG-mZVI (top), as well as fluid conductivity (σ_f), TCE and 1,1,1-TCA concentrations measured in MLS (bottom). The vertical black dashed line indicates the position of the injection well. In the electrical images, the electrodes at the surface are indicated with the black points, while the white dashed line indicates the groundwater level and the black solid lines the lithological contacts.

The electrical images in Figure 2 reveal four main units in agreement with the lithology: low electrical conductivity values at the top, characteristic of unsaturated sands; followed by a unit revealing a slight increase in σ' and σ'', corresponding to saturated sands. The highest σ' and σ'' values are observed for clayey materials in the aquitard (between 5 and 8 m bgs), and slightly lower values are associated with the deeper sandy aquifer. Furthermore, Figure 2 reveals two local anomalies in the polarization images: a shallow anomaly (between ~5 and 10 m along profile direction) characterized by high ϕ values; and a deeper anomaly (between ~10 and 20 m along profile direction) characterized by high σ'' values.

The position of the high-polarization anomalies corresponds to the region at which the highest CAHs concentrations (e.g., TCE and 1,1,1-TCA) were reported in MLS samples (Figure 2 bottom). From MLS data, the highest concentration of CAHs was measured at 4.5 m bgs (>15 mg CAHs/L), it slightly decreases for measurements at 8 m bgs (3-14 mg CAHs/L) and it further decreases for measurements at 10.5 m bgs (0.1-4 mg CAHs/L). Hence, it seems that the anomalies observed in the polarization images (ϕ and σ'') are correlated with the occurrence of high concentrations of CAHs. In detail, for the unsaturated zone, the high CAHs concentrations and the low water saturation correspond to an increase of the polarization effect and a decrease of the electrical conductivity respectively, resulting in the high ϕ values observed in Figure 2. Likewise, the occurrence of high CAHs concentrations should also explain the high-polarization (σ'') values observed between ~4 and 8 m bgs in the image of the imaginary component. The increase in both the real and imaginary components in the clayey sand materials (> 5 m bgs) leads to the observed decrease in the ϕ values in the aquitard materials, masking the response due to the high CAHs concentrations observed in the σ'' images. A recent study reported an increase in the electrical conductivity for increasing TCE concentrations in laboratory measurements[30]. However, our data reveal no correlation between σ' and TCE concentration, or between σ_f and TCE. Nevertheless, the anomalies observed in the polarization images (σ'' and ϕ) reveal correspondence with high CAHs concentrations. A previous study at the field scale also revealed a correlation between the increase in the polarization response and increasing concentrations of dissolved hydrocarbons[23, 31]. Hence, images presented in Figure 2 suggest that the geometry of the anomaly characterized by high ϕ and σ'' values is mostly controlled by the occurrence of high CAHs concentrations and not by the lithology. However, the lack of high-resolution geochemical data in the area of the aquitard (5-8 m bgs) and for areas away from the injection point impedes the confirmation of this hypothesis.

Our results show the potential of CC imaging to delimit the subsurface distribution of CAH compounds in areas where the collection of groundwater samples is not feasible. Although the objective of this study is not the delineation of the contaminant plume, a good characterization is critical for the design of the particle injection, such as defining the location for injection and sampling wells.

The uncertainty in our measurements was estimated by means of statistical analysis of the misfit between normal-reciprocal readings, as described in previous studies[28]. To assess the uncertainty in the inverted images, procedures were followed as those described in the study of Flores Orozco et al. (2013)[21]. Based on such analysis we blanked and neglected in the interpretation the areas associated with a high uncertainty (> 10%) in the inverted image, as shown in the bottom left and

right regions of the electrical images in Figure 2. A similar analysis was performed for all the imaging results presented here.

3.2. CC monitoring for delineation of GG-mZVI transport and delivery

The imaging results for the data collected during GG-mZVI injection are presented in Figure 3 in terms of the percentage change between the data collected after each injection (also 12 hours after stopping the last injection) and the baseline images (Figure 2). These monitoring images show three main aspects: 1) although a constant increase in the ϕ values is observed in the targeted area (between 8 and 10.5 m bgs), as expected due to the delivery of mZVI particles, the changes are modest (25%), even for data collected 12 h after the last injection; 2) only a minimal increase (<10%) is observed in the conductivity for aquifer sediments during the injections, which is likely related to an increase in the surface conduction due to the delivered metallic particles. However, the conductivity images ($|\sigma|$) reveal modest changes (~10%) immediately after the last injection and 12 h later, probably due to geochemical changes at the particle surfaces hindering electronic conduction; 3) an unexpected decrease is observed between 2 and 5 m bgs for both the conductivity and polarization properties, evidencing a modest decrease in the conductivity (~10%) and more pronounced change in the polarization (~50%) for data collected during GG-mZVI injection and 12 h after the last injection. The images in Figure 3 reveal that the fractures generated during the high-pressure injection were acting as preferential flow paths and allowed the GG-mZVI to migrate to shallow areas, which are mostly associated with higher porosity and lower pressure. This hypothesis is coherent with pressure logs shown in Velimirovic et al. (2014)[3], which revealed an initial peak due to opening of fractures, followed by two abrupt decreases corresponding to fracture propagation and to reaching of high permeable and lower pressure (shallow) layer, as evidenced also by the images in Figure 3.

Large ϕ variations observed in Figure 3 in the first 1 m bgs are probably artifacts resulting from computing relative changes to the values close to zero observed in the baseline image (cf. Figure 2) and will not be further discussed.
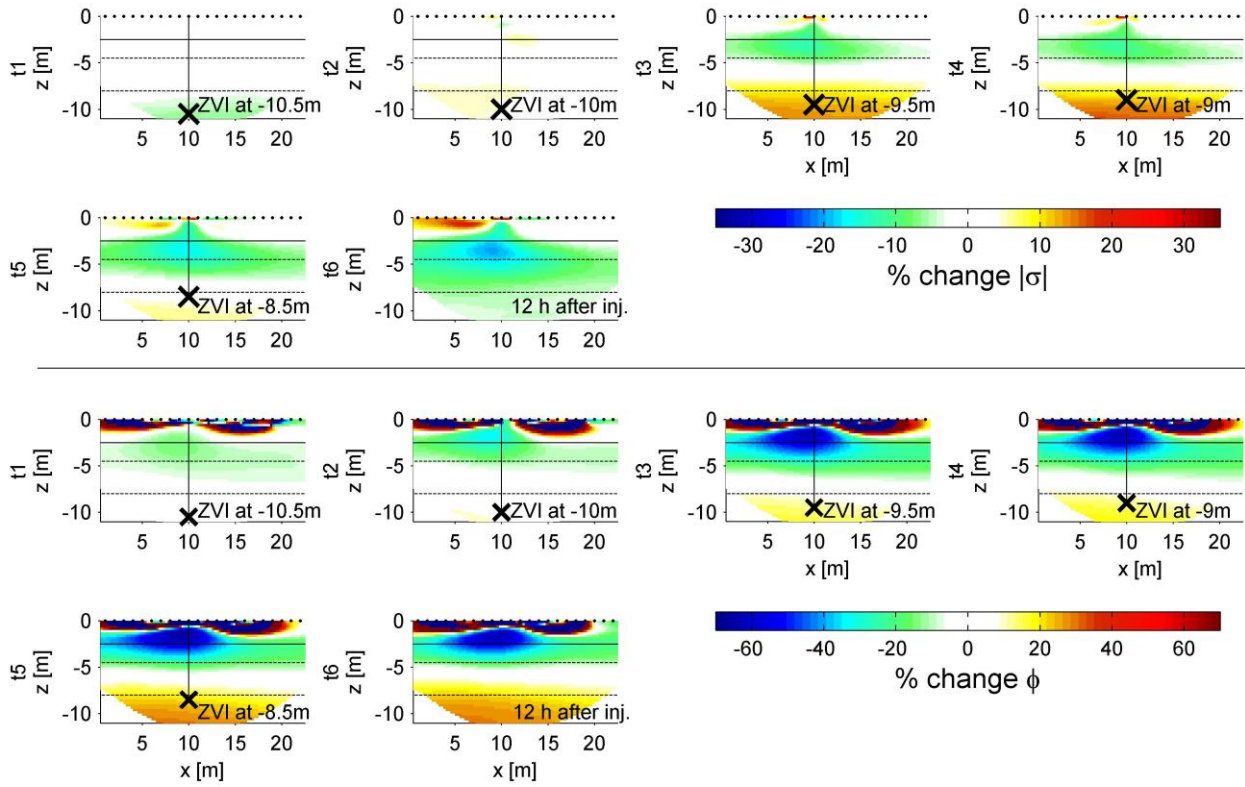
Figure 3: Relative change between the baseline (t0) images and those obtained for data collected during (t1 to t5) and after (t6) the GG-mZVI injection. The vertical line and black crosses indicate the respective positions of the injection point; black dots represent the electrodes placed at the surface, the solid horizontal line indicates the position of groundwater level; and the dashed horizontal lines indicate the upper and lower limit of the aquitard (clayey sandy materials).

Figure 4 presents pixel values extracted from the CC images at the location of the injection, as well as relevant geochemical parameters, to evaluate their correlation. The $|\sigma|$ and ϕ curves (first column in Figure 4) represent the median of pixel values extracted from the CC images at each depth in a radius of 2 m around the injection point. These curves highlight the larger changes observed in shallow areas (between 2 and 4 m bgs), in comparison with the modest variations in the aquifer sediments (between 8 and 10 m bgs). Figure 4 also presents the iron (Fe) concentrations measured in the CS collected after the injection (second column). From the six cores recovered, only CS3 revealed measurable Fe concentrations in the targeted area (~3 mg/kg). Nonetheless, measurements in CS4 and CS1 reported high Fe concentrations (>3 g/kg) between 2 and 5 m bgs, with measurements CS5 and CS6 also revealing measurable Fe concentrations in that region. Furthermore, geochemical data revealed no changes for water samples collected in the aquifer, as previously reported[3]. Changes in the geochemical parameters were observed only in samples collected at 4.5 m depth from MLS4 (Figures 4c, 4d, 4g, 4h).

The σ_f measured by means of MLS revealed minimal changes in samples collected before and after the injection. To confirm this observation, we realized measurements in the laboratory using tap water, which revealed a consistent pattern: the electrical conductivity for tap water (~54.34 mS/m) revealed only a minimal increase after the mixture with GG solutions (to ~54.54 mS/m), and only a slightly increase in the electrical conductivity (values of ~56.7 mS/m) for samples containing GG and mZVI, in mixtures with similar ratios as those injected in the field experiment. Thus, σ_f seems to be unsuitable to monitor the injection of GG-mZVI. In addition to this, we concluded that changes observed in the CC are not related to variations in the σ_f of the electrolyte. Nevertheless, similar to variations observed in the monitoring CC images, TCE and 1,1,1-TCA concentrations revealed modest changes for samples collected within the aquifer (below 8 m depth), whereas they decreased significantly at one location (MLS4) at 4.5 m depth. Furthermore, as demonstrated in previous studies[32], variations in the oxidation-reduction potential (ORP) can be used to infer the accumulation of ZVI. In this regard, our independent measurements also agree with the results observed in CC images, considering that measurements performed at the MLS4 at 4.5 m depth revealed a decrease in the ORP values, as presented in Figure 4.
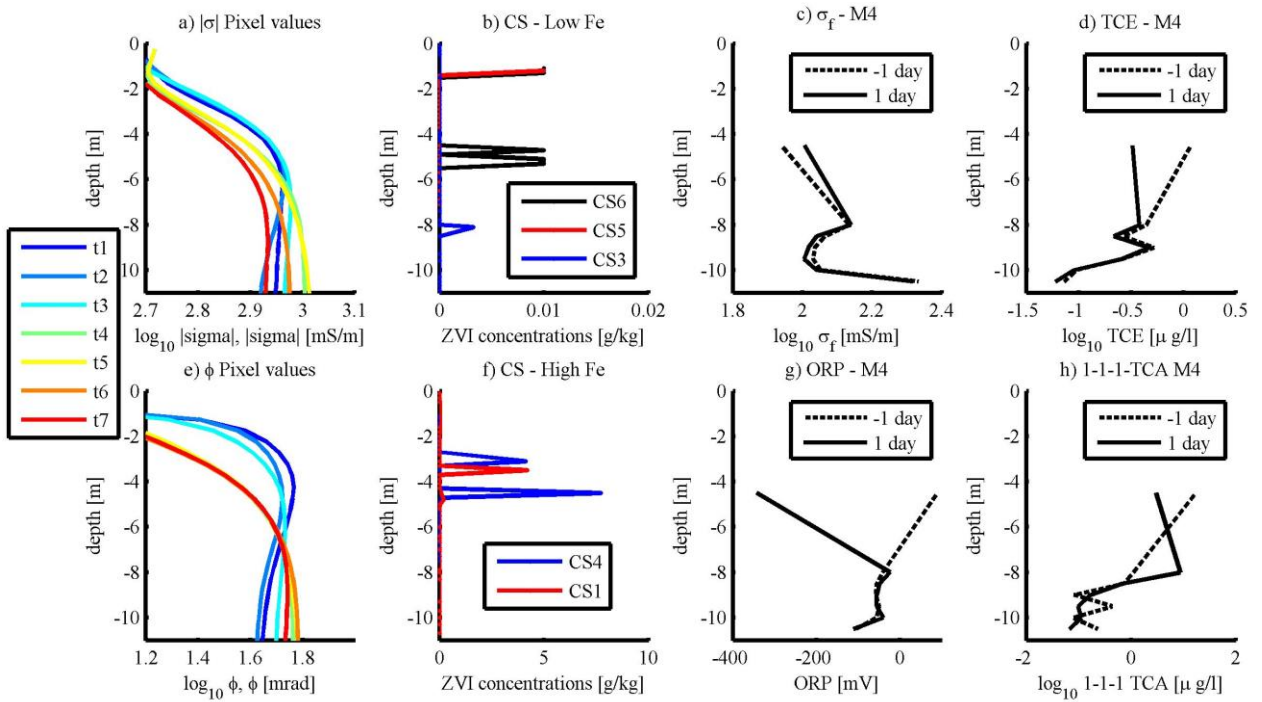

Figure 4: Comparison of geophysical and geochemical parameters. Temporal variations of conductivity (4a) and polarization (4e) at each depth can be compared with Fe-concentrations measured in the CS (4b and 4f), as well as with fluid conductivity (4c), oxidation-reduction potential (4g), as well as TCE (4d) and 1,1,1-TCA (4h) concentrations.

Both geochemical and geophysical data give evidence that the GG-mZVI was not effectively delivered into the deeper aquifer (8.5 to 10.5 m bgs), but mostly migrated into the sandy materials on the top of the aquitard. However, as a result, the CC images would be expected to exhibit an increase of the conduction and polarization response in the shallow zone due to the accumulation of metallic particles, as observed in the aquifer. The slight decrease (~10%) in the conductivity (σ' or $|\sigma|$) observed for shallow sediments, but also for deeper locations, can be explained by a reduction of the porosity due to the viscous GG clogging the pore space. The reduction in the polarization effect (ϕ) is a consequence of the GG adsorbed onto the surface of the mZVI forming the so-called "brush-layer"[33, 34] hindering electronic conduction and electrode polarization processes. Once the external electrical field is applied (i.e., current injection), the migration of ions is only taking place through the electrolyte and the brush-layer (ionic conduction), with none to minimal interactions between the ions and the metallic surface of the mZVI, i.e., no charge transfer at the electrolyte-metallic interface.

Previous studies have demonstrated a significant decrease in the zeta-potential of bare ZVI nanoparticles, after they are coated by the GG brush layer[33, 34]. In addition to this, we performed measurements in the laboratory on GG-mZVI samples with similar concentrations as those used in the field injection. These laboratory measurements revealed, as expected, low the zeta-potential values (0.37±0.07 mV), which further decreased (to -0.4±0.04 mV) after the addition of LEB-H enzymes, as those used in the field injection. Thus, the covering of the metallic surface due to the brush-layer, impeding the charge transfer mechanisms at the particles surface, explains the strong decrease observed in the polarization images (ϕ).

Samples retrieved for CS3 represent larger distances to the injection point, suggesting the development of preferential flow paths not only towards the shallow sandy materials. However, the monitoring by means of MLS was not able to track geochemical changes in that area. Nevertheless, a noticeable increase in the polarization response is observed for the aquifer materials. This response suggests the delivery of mZVI, dispersed in lower GG concentrations, as reported by Velimirovic et al. (2014)[3].

4. Outlook

CC monitoring measurements during a field GG-mZVI injection experiment provided not only information about the contaminant distribution, but also valuable information to identify the migration pathway of the injected GG-mZVI. The relatively short acquisition time permitted to obtain monitoring data with enhanced temporal resolution, i.e., after each injection (every ~15

minutes), while still covering an extended area of investigation in comparison with conventional geochemical monitoring by means of soil and water samples. Hence, CC imaging is a suitable method for the monitoring of GG-mZVI injection at the field scale. Nevertheless, geochemical data are required to fully understand the electrical signatures.

We decided to focus our investigation on the injection-period time-frame, as it is critical for the effective remediation of contaminants. In this regard, CC imaging might also be used to guide the collection of soil and water samples, following the injection, to improve the characterization of transport and fate of injected GG-mZVI.

Although not addressed here, further studies should consider the performance of 3D surveys to address the spatial variability of the CC response due to ZVI injections. The deployment of electrodes placed in boreholes might also be considered to increase the vertical resolution of the resulting electrical images, or to reach deeper areas of interest, not accessible by means of surface measurements. Future studies may also consider investigating the geophysical response due to the electrical double layer surrounding the GG-mZVI particles[35, 36]. Furthermore, CC monitoring measurements may also be performed to assess long-term changes of the geochemical properties resulting from the ZVI-driven degradation of the contaminants.

References

(1) Johnson, R.L, Nurmi. J.T, O'Brien Johnson, G.S, Fan, D., O'Brien Johnson, R.L., Shi, Z., Salter-Blanc, A.J., Tratnyek, P.G., Lowry, G.V. Field-scale transport and transformation of carboxymethylcellulose-stabilized nano zero-valent iron. *Environ. Sci. Technol.* **2013***, 47(3),* 1573-1580.

(2) Elliott, D.W., and Zhang, X.W. Field Assessment of Nanoscale Bimetallic Particles for Groundwater Treatment. *Environ. Sci. Technol.* **2001**, *35*, 4922-4926.

(3) Velimirovic, M. Tosco, T., Uytteboek, M., Luna, M., Gastone, F., De Boer, C., Klaas, N., Spaion, H., Eisenmann, H., Lasson, P.O., Braun, J., Sethi, R., Bastiaens, L. Field assessment of guar gum stabilized microscale zerovalent iron particles for in-situ remediation of 1,1,1-trichloroethane. *Journal of Contaminated Hydrology* **2014**, 164: 88-99.

(4) Tosco, T.; Petrangeli Papini, M.; Cruz Viggi, C.; Sethi, R. Nanoscale iron particles for groundwater remediation: a review. *Journal of Cleaner Production* **2014**, *77*, 10-21.

(5) Grieger, K.D., Fjordboge, A., Hartmann, N.B., Eriksson, E., Bjerg, P.L., and Baun, A. Environmental benefits and risks of zero-valent iron nanoparticles (nZVI) for in situ remediation: Risk mitigation or trade-off? *Journal of Contaminant Hydrology* **2010**, *118*, 165-183.

(6) Tosco, T., and Sethi, R. Transport of non-newtonian suspension of highly concentrated mico- and nanoscale ison particles in porous media: a modeling approach. *Environ. Sci. Technol.* **2010**, *44(23)*, 9062, 9068

(7) Velimirovic, M., Larsson, P.O., Simons, Q., and Bastiaens, L. Reactivity screening of microscale zerovalent irons and iron sulfides towards different CAHs under standardized experimental conditions, *J. Hazard. Mater*. **2013**, *252-253*, 204-212.

(8) Phenrat, T., Saleh, N., Sirk, K., Tilton, R., D., Lowry, G., V. Aggregation and sedimentation of aqueous nanoscale zerovalent iron dispersions. *Environ. Sci. Technol.* **2007**, 41 284-290.

(9) Phenrat, T., Kim, H.J., Fagerlund, F., Illangasekare, T., Tilton, R.D., Lowry, G.V. Particle Size Distribution, Concentration, and Magnetic Attraction Affect Transport of Polymer-modified Fe0 Nanoparticles in Sand Columns. *Environ. Sci. Technol.* **2009**, 43 (13), 5079–5085.

(10) Dalla Vecchia, E., Luna, M. and Sethi, R. Transport in Porous Media of Highly Concentrated Iron Micro- and Nanoparticles in the Presence of Xanthan Gum. *Environ. Sci. Technol.* **2009**, 43(23), 8942-8947.

(11) Gastone, F.; Tosco, T.; Sethi, R. 2014. Green stabilization of microscale iron particles using guar gum: bulk rheology, sedimentation rate and enzymatic degradation. *Journal of Colloid and Interface Science* **2014**, *421*, 33-43.

(12) Velimirovic, M., Carniato, L., Simons, Q., Schoups, G., Seuntjens, P. and Bastiaens, L. Corrosion rate estimations of microscale zerovalent iron particles via direct hydrogen production measurements. *Journal of Hazardous Materials* **2014**, 270: 18-26.

(13) Saleh, N., Sirk, K., Liu, Y., Phenrat, T., Dufour, B., Matyjaszewski, K., Tilton, R.D., Lowry, G.V. Surface modifications enhance nanoiron transport and NAPL targeting in saturated porous media. *Environmental Engineering Science* **2007***, 24*, 45-57.

(14) Tosco, T.; Gastone, F.; Sethi, R. Guar gum solutions for improved delivery of iron particles in porous media (Part 2): Iron transport tests and modeling in radial geometry. *Journal of Contaminant Hydrology* **2014**, *166(0)*, 34-51.

(15) Phenrat, T., Cihan, A., Kim, H.J., Mital, M., Illangasekare, T., Lowry, G. V. Transport and Deposition of Polymer-Modified Fe0 Nanoparticles in 2-D Heterogeneous Porous Media: Effects of Particle Concentration, Fe0 Content, and Coatings. *Environ. Sci. Technol.* **2010**, 44 (23), 9086–9093.

(16) Raychoudhury, T., Tufenkj, N., Ghoshal, S. Aggregation and deposition kinetics of carboxymethyl cellulose-modified zero-valent iron nanoparticles in porous media. *Water Research* **2012**, *46(6)*, 1735-1744.

(17) Kemna, A., Binley, A., Cassiani, G., Niederleithinger, E., Revil, A., Slater, L., Williams, H.K., Flores Orozco, A., Haegel, F.-H., Hördt, A., Kruschwitz, S., Leroux, V., Titov, K., and Zimmermann, E. An overview of the spectral induced polarization method for near-surface applications. *Near Surface Geophysics* **2013**, *10(6),* 453-468.

(18) Wong, J. An electrochemical model of the induced polarization phenomenon in disseminated sulfide ores. *Geophysics* **1979**, *44(7)*, 1245-1265.

(19) Slater, L., and Binley, A. Synthetic and field-based electrical imaging of a zerovalent iron barrier: Implications for monitoring long-term barrier performance. *Geophysics* **2006**, *71*, B129-B137.

(20) Williams, K.H., Ntarlagiannis, D., Slater, L.D., Dohnalkova, A., Hubbard, S.S., and Banfield, J.F. Geophysical imaging of stimulated microbial biomineralization. *Environ. Sci. Technol.* **2005**, *39*, 7592-7600.

(21) Flores Orozco, A., Williams, H.K., and Kemna, A. Time-lapse spectral induced polarization imaging of stimulated uranium bioremediation. *Near Surface Geophysics* **2013**, *11*, 531-544. doi:10.3997/1873-0604.2013020.

(22) Flores Orozco, A., Williams, K.H., Long, P.E., Hubbard, S.S., and Kemna, A. Using complex resistivity imaging to infer biogeochemical processes associated with bioremediation of a uranium-contaminated aquifer. *Journal of Geophysical Research* **2011**, *116*, G03001.

(23) Flores Orozco, A., Kemna, A., Oberdörster, C., Zschornack, L., Leven, C., Dietrich, P., and Weiss, H. Delineation of subsurface hydrocarbon contamination at a former hydrogenation plant using spectral induced polarization imaging. *Journal of Contaminant Hydrology*, **2012**, *136-137*, 131-144.

(24) Joyce, R.A., Glaser Ii, D.R., Werkema Jr, D.D., and Atekwana, E.A. Spectral induced polarization response to nanoparticles in a saturated sand matrix. *Journal of Applied Geophysics* **2012**, *77*, 63-71.

(25) Velimirovic, M., Chen, H., Simons, Q., Bastiaens, L. Reactivity recovery of guar gum coupled mZVI by means of enzymatic breakdown and rinsing. *J. Contam. Hydrol.* **2012,** *142-143,* 1-10.

(26) Archie, G.E. The electrical resistivity log as an aid in determining some reservoir characteristics". *Petroleum Transactions of AIME* **1942**, *146*, 54–62.

(27) Kemna, A., 2000 Tomographic inversion of complex resistivity – theory and application: Ph.D. thesis, Ruhr University of Bochum.

(28) Flores Orozco, A., Kemna, A., and Zimmermann, E. Data error quantification in spectral induced polarization imaging. *Geophysics* **2012**, *77 (3),* E227-E237.

(29) Blaschek, R., Hördt, A., and Kemna, A. A new sensitivity-controlled focusing regularization scheme for the inversion of induced polarization data based on the minimum gradient support. *Geophysics* **2012**, *73,* F45-F54.

(30) Hort, R. D., Revil, A., and Munakata-Marr, J. Analysis of sources of bulk conductivity change in saturated silica sand after unbuffered TCE oxidation by permanganate. *Journal of Contaminant Hydrology* **2012**, *165*, 11-23.

(31) Kemna, A, Binley, A., and Slater, L. Crosshole IP imaging for engineering and environmental applications. *Geophysics* **2004**, *69*, 97-107.

(32) Shi, Z., Nurmi, J.T., and Tratnyek, G.P. Effects of Nano Zero-Valent Iron on Oxidation−Reduction Potential. *Environ. Sci. Technol.* **2011**, 45 (4), 1586–1592

(33) Tiraferri, A., Chen, K. L., Sethi, R., and Elimelech, M. Reduced aggregation and sedimentation of zero-valent iron nanoparticles in the presence of guar gum. *Journal of Colloid and Interface Science* **2008**, *324(1)*, 71-79.

(34) Tiraferri, A.; Sethi, R. Enhanced transport of zerovalent iron nanoparticles in saturated porous media by guar gum. *Journal of Nanoparticle Research,* **2009**, *11(3),* 635-645.

(35) Louie, S.M., Phenrat, T., Small, M.J., Tilton, R.D., Lowry, G.V. Parameter identifiability in application of soft Particle Electrokinetic Theory to determine polymer and polyelectrolyte coating thicknesses on colloids. *Langmuir* **2012**, 28 (28), 10334–10347

(36) Phenrat, T., Saleh, N., Sirk, K., Kim, H.J., Tilton, R., D., Lowry, G., V. Stabilization of aqueous nanoscale zerovalent iron dispersions by anionic polyelectrolytes: adsorbed anionic polyelectrolyte layer properties and their effect on aggregation and sedimentation. *Journal of Nanoparticle Research* **2008**, 10, 795-814.

Before injection

12 h after mZVI injection